LAWRENCE
LIVERMORE
NATIONAL
LABORATORY

Conservation Laws for Coupled Hydro-mechanical Processes in Unsaturated Porous Media: Theory and Implementation

R. I. Borja, J. A. White

February 19, 2010

Mechanics of Unsaturated Geomaterials

Disclaimer

This document was prepared as an account of work sponsored by an agency of the United States government. Neither the United States government nor Lawrence Livermore National Security, LLC, nor any of their employees makes any warranty, expressed or implied, or assumes any legal liability or responsibility for the accuracy, completeness, or usefulness of any information, apparatus, product, or process disclosed, or represents that its use would not infringe privately owned rights. Reference herein to any specific commercial product, process, or service by trade name, trademark, manufacturer, or otherwise does not necessarily constitute or imply its endorsement, recommendation, or favoring by the United States government or Lawrence Livermore National Security, LLC. The views and opinions of authors expressed herein do not necessarily state or reflect those of the United States government or Lawrence Livermore National Security, LLC, and shall not be used for advertising or product endorsement purposes.

Conservation laws for coupled hydro-mechanical processes in unsaturated porous media: Theory and implementation

Ronaldo I. Borja* · Joshua A. White†

*Department of Civil and Environmental Engineering, Stanford University,
 Stanford, CA 94305, USA
 E-mail: `borja@stanford.edu`
†Computational Geosciences Group, Lawrence Livermore National Laboratory,
 Livermore, CA 94551, USA
 E-mail: `jawhite@llnl.gov`

Summary. We develop conservation laws for coupled hydro-mechanical processes in unsaturated porous media using three-phase continuum mixture theory. From the first law of thermodynamics, we identify energy-conjugate variables for constitutive modeling at macroscopic scale. Energy conjugate expressions identified relate a certain measure of effective stress to the deformation of the solid matrix, the degree of saturation to the matrix suction, the pressure in each constituent phase to the corresponding intrinsic volume change of this phase, and the seepage forces to the corresponding pressure gradients. We then develop strong and weak forms of boundary-value problems relevant for 3D finite element modeling of coupled hydro-mechanical processes in unsaturated porous media. The paper highlights a 3D numerical example illustrating the advances in the solution of large-scale coupled finite element systems, as well as the challenges in developing more predictive tools satisfying the basic conservation laws and the observed constitutive responses for unsaturated porous materials.

1 Introduction

A portion of Earth's crust between the land surface and the phreatic zone consists of a three-phase solid-water-air system called the vadose, or unsaturated, zone [18]. Water in the vadose zone has a pressure head less than atmospheric pressure, and is retained by both capillary action and adhesion [17]. Movement of water within the vadose zone is governed by coupled hydro-mechanical conservation laws, as well as by a set of constitutive equations. The Richards equation [21] is often used to mathematically describe the flow of water, based partially on Darcy's law. However, this equation does not account for solid deformation that could impact, for instance, the stability of unsaturated slopes.

Coupling of hydro-mechanical processes may have a significant impact on the performance of civil infrastructures built on or within an unsaturated region. Collapse of the solid matrix could be triggered by the loss of capillary pressure due to increased saturation, as well as by frictional drag exerted by the fluid on the solid matrix in the presence of fluid flow. Conversely, deformation of the solid matrix, particularly when dominated by extreme volume changes, could induce significant changes in the fluid pressures and degree of saturation. In addition to coupled hydro-mechanical processes, constitutive responses in unsaturated porous materials are also known to be very complex. Deformation responses of the sediments are generally inelastic and hysteretic. Furthermore, the wetting and drying portions of the water retention curve are not the same, suggesting that a different form of hysteresis may have to be considered for modeling complex sequences of wetting and drying.

In this paper we review the conservation laws governing the coupled hydro-mechanical processes in unsaturated porous media, including the balance of mass and balance of momentum for all the constituent phases. There is no unique set of independent variables that one may choose for the formulation, and here we select the displacement of the solid matrix and the pore water and pore air pressures as the preferred independent variables. We use the first and second laws of thermodynamics to infer an appropriate measure of effective stress for the solid deformation response, as well as identify other sets of energy-conjugate variables relevant for developing hydro-mechanical constitutive laws.

For the numerical implementation of the conservation laws, we employ a mixed finite element formulation utilizing stabilized low-order mixed finite elements in 2D and 3D [9, 27]. The underlying rationale for choosing a low-order interpolation is to accommodate spatially varying material and geometric conditions. Sources of spatial heterogeneity include the irregular topography and spatially varying properties of the sediments, as well as the typically complex boundary conditions. However, low-order finite elements, particularly those employing equal-order interpolation of displacement and pressure fields, have a propensity to exhibit pressure oscillation in the limit of full saturation and undrained loading. To circumvent the unstable behavior of these low-order mixed finite elements, we employ a polynomial pressure projection stabilization [4, 5, 12].

A numerical example is presented toward the end of this chapter illustrating how the developed conservation laws may be used for large-scale simulation of boundary-value problems in unsaturated porous materials. Coupling of the degrees of freedom is more intricate in the unsaturated case than in the fully saturated case. For example, the discrete gradient and discrete divergence operators in the coupled system are strongly dependent on the degree of saturation, whereas they are constant in the fully saturated case. Thus, additional terms arise in the linearization of the coupled system. Furthermore, direct solvers may not be feasible for very large systems, and iterative solvers may need to be used. The numerical example aims to highlight the advances

and challenges in solving coupled systems of equations in unsaturated porous mechanics.

2 Mass and momentum conservation laws

We consider a mixture consisting of a solid matrix with continuous voids filled with water and air. The total volume of the mixture is $V = V_s + V_w + V_a$ and the total mass is $M = M_s + M_w + M_a$, where $M_\alpha = \rho_\alpha V_\alpha$ for $\alpha =$ solid, water, and air; and ρ_α is the true mass density of the α constituent. The volume fraction occupied by the α constituent is given by $\phi_\alpha = V_\alpha / V$, which gives

$$\phi^s + \phi^w + \phi^a = 1 . \tag{1}$$

The partial mass density of the α constituent is given by $\rho^\alpha = \phi^\alpha \rho_\alpha$, where ρ_α is the intrinsic mass density of the α constituent. This gives

$$\rho^s + \rho^w + \rho^a = \rho , \tag{2}$$

where $\rho = M/V$ is the total mass density of the mixture.

We denote the instantaneous intrinsic velocities of the solid, water, and air constituents by $\boldsymbol{v} \equiv \boldsymbol{v}_s$, $\boldsymbol{v}_w$, and $\boldsymbol{v}_a$, respectively. The material time derivative following the solid motion is denoted by the symbol

$$\frac{\mathrm{d}(\cdot)}{\mathrm{d}t} = \frac{\partial(\cdot)}{\partial t} + \boldsymbol{\nabla} \cdot \boldsymbol{v} . \tag{3}$$

In the absence of mass exchanges among the three constituents, balance of mass for the solid, water, and air constituents, respectively, takes the form

$$\frac{\mathrm{d}\rho^s}{\mathrm{d}t} + \rho^s \boldsymbol{\nabla} \cdot \boldsymbol{v} = 0 , \tag{4}$$

$$\frac{\mathrm{d}\rho^w}{\mathrm{d}t} + \rho^w \boldsymbol{\nabla} \cdot \boldsymbol{v} = -\boldsymbol{\nabla} \cdot \boldsymbol{w}^w , \tag{5}$$

$$\frac{\mathrm{d}\rho^w}{\mathrm{d}t} + \rho^a \boldsymbol{\nabla} \cdot \boldsymbol{v} = -\boldsymbol{\nabla} \cdot \boldsymbol{w}^a , \tag{6}$$

where $\boldsymbol{w}^\alpha$ (for $\alpha =$ water, air) is the Eulerian relative flow vector of the α constituent with respect to the solid matrix, and is given explicitly by the relations

$$\boldsymbol{w}^\alpha = \rho^\alpha \widetilde{\boldsymbol{v}}_\alpha , \qquad \widetilde{\boldsymbol{v}}_\alpha = \boldsymbol{v}_\alpha - \boldsymbol{v} , \qquad \alpha = w, a . \tag{7}$$

Barotropic flows satisfy functional relations of the form

$$f_\alpha(p_\alpha, \rho_\alpha) = 0 , \qquad \alpha = s, w, a , \tag{8}$$

where p_α denotes the intrinsic pressure equal to the actual force per unit actual area acting on the α constituent. The functional relations given above determine the intrinsic bulk modulus for the α constituent as

$$K_\alpha = \rho_\alpha p'_\alpha(\rho_\alpha), \qquad \alpha = \text{s}, \text{w}, \text{a}. \tag{9}$$

In this case, the mass conservation laws specialize to the form

$$\frac{\mathrm{d}\phi^\text{s}}{\mathrm{d}t} + \frac{\phi^\text{s}}{K_\text{s}} \frac{\mathrm{d}p_\text{s}}{\mathrm{d}t} + \phi^\text{s} \boldsymbol{\nabla} \cdot \boldsymbol{v} = 0, \tag{10}$$

$$\frac{\mathrm{d}\phi^\text{w}}{\mathrm{d}t} + \frac{\phi^\text{w}}{K_\text{w}} \frac{\mathrm{d}p_\text{w}}{\mathrm{d}t} + \phi^\text{w} \boldsymbol{\nabla} \cdot \boldsymbol{v} = -\frac{1}{\rho_\text{w}} \boldsymbol{\nabla} \cdot \boldsymbol{w}^\text{w}, \tag{11}$$

$$\frac{\mathrm{d}\phi^\text{a}}{\mathrm{d}t} + \frac{\phi^\text{a}}{K_\text{a}} \frac{\mathrm{d}p_\text{a}}{\mathrm{d}t} + \phi^\text{a} \boldsymbol{\nabla} \cdot \boldsymbol{v} = -\frac{1}{\rho_\text{a}} \boldsymbol{\nabla} \cdot \boldsymbol{w}^\text{a}. \tag{12}$$

We introduce void fractions ψ^w and ψ^a representing the ratios between the volumes of water and air in the voids, respectively, to the total volume of the void itself. They are related to the volume fractions as

$$\psi^\text{w} = \frac{\phi^\text{w}}{1 - \phi^\text{s}}, \qquad \psi^\text{a} = \frac{\phi^\text{a}}{1 - \phi^\text{s}}, \qquad \psi^\text{w} + \psi^\text{a} = 1, \tag{13}$$

where ψ^w is the degree of saturation. Taking the derivatives and substituting into (11) and (12) gives

$$(1 - \phi^\text{s})\frac{\mathrm{d}\psi^\text{w}}{\mathrm{d}t} + \frac{\phi^\text{w}}{K_\text{w}} \frac{\mathrm{d}p_\text{w}}{\mathrm{d}t} + \frac{\psi^\text{w}\phi^\text{s}}{K_\text{s}} \frac{\mathrm{d}p_\text{s}}{\mathrm{d}t} + \psi^\text{w} \boldsymbol{\nabla} \cdot \boldsymbol{v} = -\frac{1}{\rho_\text{w}} \boldsymbol{\nabla} \cdot \boldsymbol{w}^\text{w}, \tag{14}$$

$$(1 - \phi^\text{s})\frac{\mathrm{d}\psi^\text{a}}{\mathrm{d}t} + \frac{\phi^\text{a}}{K_\text{a}} \frac{\mathrm{d}p_\text{a}}{\mathrm{d}t} + \frac{\psi^\text{a}\phi^\text{s}}{K_\text{s}} \frac{\mathrm{d}p_\text{s}}{\mathrm{d}t} + \psi^\text{a} \boldsymbol{\nabla} \cdot \boldsymbol{v} = -\frac{1}{\rho_\text{a}} \boldsymbol{\nabla} \cdot \boldsymbol{w}^\text{a}. \tag{15}$$

Next, we consider a functional relationship for p_s of the form

$$p_\text{s} = \widetilde{p}_\text{s}(\rho^\text{s}, \phi^\text{s}) \neq \widetilde{p}_\text{s}(\rho^\text{s}/\phi^\text{s}). \tag{16}$$

The above equation defines an elastic compressibility law for the solid matrix. Note that the functional relationship $p_\text{s} = \widetilde{p}_\text{s}(\rho^\text{s}/\phi^\text{s}) = \widetilde{p}_\text{s}(\rho_\text{s})$ defines the elastic compressibility law for the solid constituent, and is a redundant expression. We thus assume in (16) that the functional relationship for p_s depends on ρ^s and ϕ^s, but not through $\rho^\text{s}/\phi^\text{s}$. Taking the material time derivative of (16) gives

$$\frac{\mathrm{d}p_\text{s}}{\mathrm{d}t} = \frac{\partial \widetilde{p}_\text{s}}{\partial \rho^\text{s}} \frac{\mathrm{d}\rho^\text{s}}{\mathrm{d}t} + \frac{\partial \widetilde{p}_\text{s}}{\partial \phi^\text{s}} \frac{\mathrm{d}\phi^\text{s}}{\mathrm{d}t}. \tag{17}$$

But

$$\frac{1}{\rho^\text{s}} \frac{\mathrm{d}\rho^\text{s}}{\mathrm{d}t} = \frac{\mathrm{d}}{\mathrm{d}t}\left[\ln\left(\frac{\rho^\text{s}}{\rho_0^\text{s}}\right)\right] = \frac{\mathrm{d}}{\mathrm{d}t}(\ln J^{-1}) = -\boldsymbol{\nabla} \cdot \boldsymbol{v}, \tag{18}$$

where $\rho_0^\text{s} = J\rho^\text{s}$ is the partial mass density for solid in the reference configuration. Together with (10), equation (17) gives

$$\phi^\text{s}\frac{\mathrm{d}p_\text{s}}{\mathrm{d}t} = -K\boldsymbol{\nabla} \cdot \boldsymbol{v}, \tag{19}$$

where

$$K = \phi^{\mathrm{s}}\left(\rho^{\mathrm{s}}\frac{\partial \widetilde{p}_{\mathrm{s}}}{\partial \rho^{\mathrm{s}}} + \phi^{\mathrm{s}}\frac{\partial \widetilde{p}_{\mathrm{s}}}{\partial \phi^{\mathrm{s}}}\right)\bigg/\left(1 + \frac{\partial \widetilde{p}_{\mathrm{s}}}{\partial \phi^{\mathrm{s}}}\frac{\phi^{\mathrm{s}}}{K_{\mathrm{s}}}\right) \tag{20}$$

is the elastic bulk modulus of the solid matrix. Substituting (19) into (10), (14) and (15) gives

$$\frac{\mathrm{d}\phi^{\mathrm{s}}}{\mathrm{d}t} + (B - 1 + \phi^{\mathrm{s}})\boldsymbol{\nabla}\cdot\boldsymbol{v} = 0\,, \tag{21}$$

$$(1 - \phi^{\mathrm{s}})\frac{\mathrm{d}\psi^{\mathrm{w}}}{\mathrm{d}t} + \frac{\phi^{\mathrm{w}}}{K_{\mathrm{w}}}\frac{\mathrm{d}p_{\mathrm{w}}}{\mathrm{d}t} + \psi^{\mathrm{w}}B\boldsymbol{\nabla}\cdot\boldsymbol{v} = -\frac{1}{\rho_{\mathrm{w}}}\boldsymbol{\nabla}\cdot\boldsymbol{w}^{\mathrm{w}}\,, \tag{22}$$

$$(1 - \phi^{\mathrm{s}})\frac{\mathrm{d}\psi^{\mathrm{a}}}{\mathrm{d}t} + \frac{\phi^{\mathrm{a}}}{K_{\mathrm{a}}}\frac{\mathrm{d}p_{\mathrm{a}}}{\mathrm{d}t} + \psi^{\mathrm{a}}B\boldsymbol{\nabla}\cdot\boldsymbol{v} = -\frac{1}{\rho_{\mathrm{a}}}\boldsymbol{\nabla}\cdot\boldsymbol{w}^{\mathrm{a}}\,, \tag{23}$$

where

$$B = 1 - \frac{K}{K_{\mathrm{s}}} \tag{24}$$

is the Biot coefficient.

Balance of linear momentum in the absence of inertia forces may be written for a solid-water-air mixture as

$$\boldsymbol{\nabla}\cdot\boldsymbol{\sigma}^{\mathrm{s}} + \rho^{\mathrm{s}}\boldsymbol{g} + \boldsymbol{h}^{\mathrm{s}} = \boldsymbol{0}\,, \tag{25}$$

$$\boldsymbol{\nabla}\cdot\boldsymbol{\sigma}^{\mathrm{w}} + \rho^{\mathrm{w}}\boldsymbol{g} + \boldsymbol{h}^{\mathrm{w}} = \boldsymbol{0}\,, \tag{26}$$

$$\boldsymbol{\nabla}\cdot\boldsymbol{\sigma}^{\mathrm{a}} + \rho^{\mathrm{a}}\boldsymbol{g} + \boldsymbol{h}^{\mathrm{a}} = \boldsymbol{0}\,, \tag{27}$$

where $\boldsymbol{\sigma}^{\mathrm{s}}$, $\boldsymbol{\sigma}^{\mathrm{w}}$, and $\boldsymbol{\sigma}^{\mathrm{a}}$ are the partial Cauchy stress tensors defined as the ratio between the forces acting on solid, water, and air, respectively, per unit area of the mixture. The partial stresses satisfy the relation

$$\boldsymbol{\sigma}^{\mathrm{s}} + \boldsymbol{\sigma}^{\mathrm{w}} + \boldsymbol{\sigma}^{\mathrm{a}} = \boldsymbol{\sigma}\,, \tag{28}$$

where $\boldsymbol{\sigma}$ is the total Cauchy stress tensor. The body force density vectors $\boldsymbol{h}^{\mathrm{s}}$, $\boldsymbol{h}^{\mathrm{w}}$, and $\boldsymbol{h}^{\mathrm{a}}$ act on the solid, water, and air constituents, respectively, measured with respect to the total volume of the mixture, and satisfy the closure condition

$$\boldsymbol{h}^{\mathrm{s}} + \boldsymbol{h}^{\mathrm{w}} + \boldsymbol{h}^{\mathrm{a}} = \boldsymbol{0}\,. \tag{29}$$

Balance of linear momentum for the entire mixture thus takes the form

$$\boldsymbol{\nabla}\cdot\boldsymbol{\sigma} + \rho\boldsymbol{g} = \boldsymbol{0}\,, \tag{30}$$

where $\boldsymbol{g}$ is the gravity acceleration vector.

3 Balance of energy and the effective stress

Imposing the first law of thermodynamics on a solid-water-air mixture yields the following expression for the material time derivative of internal energy [6–8]

$$\rho\dot{e} = \boldsymbol{\sigma}^{\mathrm{s}} : \boldsymbol{d} + \boldsymbol{\sigma}^{\mathrm{w}} : \boldsymbol{d}_{\mathrm{w}} + \boldsymbol{\sigma}^{\mathrm{a}} : \boldsymbol{d}_{\mathrm{a}} + r - \boldsymbol{\nabla} \cdot \boldsymbol{q} \,, \tag{31}$$

where $\boldsymbol{d}$, $\boldsymbol{d}_{\mathrm{w}}$, and $\boldsymbol{d}_{\mathrm{a}}$ are the rates of deformation for the solid, water, and air constituents, respectively, r is the heat supply per unit volume of the mixture, and $\boldsymbol{q}$ is the heat flux vector. If we assume that $\boldsymbol{\sigma}^{\mathrm{w}}$ and $\boldsymbol{\sigma}^{\mathrm{a}}$ are isotropic tensors of the form

$$\boldsymbol{\sigma}^{\mathrm{w}} = -\phi^{\mathrm{w}} p_{\mathrm{w}} \boldsymbol{1} \,, \qquad \boldsymbol{\sigma}^{\mathrm{a}} = -\phi^{\mathrm{a}} p_{\mathrm{a}} \boldsymbol{1} \,, \tag{32}$$

where $\boldsymbol{1}$ is the second-order identity tensor (Kronecker delta), then we get

$$\rho\dot{e} = \boldsymbol{\sigma}^{\mathrm{s}} : \boldsymbol{d} - \phi^{\mathrm{w}} p_{\mathrm{w}} \boldsymbol{\nabla} \cdot \boldsymbol{v}_{\mathrm{w}} - \phi^{\mathrm{a}} p_{\mathrm{a}} \boldsymbol{\nabla} \cdot \boldsymbol{v}_{\mathrm{a}} + r - \boldsymbol{\nabla} \cdot \boldsymbol{q} \,, \tag{33}$$

where $\boldsymbol{v}_{\mathrm{w}}$ and $\boldsymbol{v}_{\mathrm{a}}$ are the velocities of water and air constituents, respectively. Adding the null scalar product $(\boldsymbol{\sigma} - \boldsymbol{\sigma}^{\mathrm{s}} - \boldsymbol{\sigma}^{\mathrm{w}} - \boldsymbol{\sigma}^{\mathrm{a}}) : \boldsymbol{d}$ to this expression gives

$$\rho\dot{e} = \boldsymbol{\sigma} : \boldsymbol{d} - \phi^{\mathrm{w}} p_{\mathrm{w}} \boldsymbol{\nabla} \cdot \widetilde{\boldsymbol{v}}_{\mathrm{w}} - \phi^{\mathrm{a}} p_{\mathrm{a}} \boldsymbol{\nabla} \cdot \widetilde{\boldsymbol{v}}_{\mathrm{a}} + r - \boldsymbol{\nabla} \cdot \boldsymbol{q} \,, \tag{34}$$

where $\widetilde{\boldsymbol{v}}_{\mathrm{w}}$ and $\widetilde{\boldsymbol{v}}_{\mathrm{a}}$ are the relative velocities of water and air constituents defined earlier in (7).

The divergence of the relative velocity $\widetilde{\boldsymbol{v}}_{\alpha}$ can be expressed in terms of the divergence of the Eulerian relative flow vector $\boldsymbol{w}^{\alpha}$ as

$$\boldsymbol{\nabla} \cdot \boldsymbol{w}^{\alpha} = \phi^{\alpha} \rho_{\alpha} \boldsymbol{\nabla} \cdot \widetilde{\boldsymbol{v}}_{\alpha} + \widetilde{\boldsymbol{v}}_{\alpha} \cdot \boldsymbol{\nabla}(\phi^{\alpha} \rho_{\alpha}) \,, \qquad \alpha = \mathrm{w}, \mathrm{a} \,. \tag{35}$$

Solving for $\boldsymbol{\nabla} \cdot \widetilde{\boldsymbol{v}}_{\alpha}$ from the above equation and using (22) and (23), we obtain the following alternative expression for the rate of change of internal energy

$$\rho\dot{e} = \boldsymbol{\sigma}' : \boldsymbol{d} - s(1 - \phi^{\mathrm{s}}) \frac{\mathrm{d}\psi^{\mathrm{w}}}{\mathrm{d}t} + \mathcal{A} + \mathcal{G} + r - \boldsymbol{\nabla} \cdot \boldsymbol{q} \,, \tag{36}$$

where

$$\boldsymbol{\sigma}' = \boldsymbol{\sigma} + B\bar{p}\boldsymbol{1} \,, \tag{37}$$

$$\bar{p} = \psi^{\mathrm{w}} p_{\mathrm{w}} + \psi^{\mathrm{a}} p_{\mathrm{a}} = \psi^{\mathrm{w}} p_{\mathrm{w}} + (1 - \psi^{\mathrm{w}}) p_{\mathrm{a}} \,, \tag{38}$$

$$s = p_{\mathrm{a}} - p_{\mathrm{w}} \,, \tag{39}$$

and

$$\mathcal{A} = \sum_{\alpha = \mathrm{w}, \mathrm{a}} \frac{\phi^{\alpha}}{K_{\alpha}} \frac{\mathrm{d}p_{\alpha}}{\mathrm{d}t} p_{\alpha} \,, \tag{40}$$

$$\mathcal{G} = \sum_{\alpha = \mathrm{w}, \mathrm{a}} \left(\frac{1}{\rho_{\alpha}} \boldsymbol{\nabla} \cdot \boldsymbol{w}^{\alpha} - \phi^{\alpha} \boldsymbol{\nabla} \cdot \widetilde{\boldsymbol{v}}_{\alpha} \right) p_{\alpha} \,, \tag{41}$$

Equation (36) identifies $\boldsymbol{\sigma}'$ as the stress tensor that is energy-conjugate to the rate of deformation of the solid matrix, $\boldsymbol{d}$; and the suction stress s as energy-conjugate to the rate of change of degree of saturation, $\mathrm{d}\psi^{\mathrm{w}}/\mathrm{d}t$. The energy-conjugacy between the intrinsic pressures in water and air and the rates of change of their respective intrinsic volumes are represented by the

term $\mathcal{A}$. Finally, the term $\mathcal{G}$ represents the rate of energy expended by the fluid pressures in either injecting or expelling fluids relative to the solid matrix.

Equation (37) is the 'effective stress equation' for the partially saturated porous material. It is very similar in form to Skempton's [24] equation except that he used Bishop's [3] parameter χ in lieu of degree of saturation ψ^{w} for the mean neutral stress $\overline{p}$. The ratio K/K_{s} is typically in the range 0.1–0.5 for saturated rocks and concrete [24], and so, Biot's coefficient B ranges from 0.9–0.5 for such materials. For soils, however, K/K_{s} is very small, and so it is customary to take $B = 1.0$ for such material, resulting in the following expression for the effective stress similar to that developed in [23**?**]

$$\boldsymbol{\sigma}' = \boldsymbol{\sigma} + \left[\psi^{\mathrm{w}}p_{\mathrm{w}} + (1 - \psi^{\mathrm{w}})p_{\mathrm{a}}\right]\mathbf{1}\,. \tag{42}$$

On the other hand, if $\psi^{\mathrm{w}} = 1$ (fully saturated), the effective stress equation becomes

$$\boldsymbol{\sigma}' = \boldsymbol{\sigma} + Bp_{\mathrm{w}}\mathbf{1}\,. \tag{43}$$

This equation was shown by Nur and Byerlee [19] to be theoretically exact for saturated rocks. Finally, we recover Terzaghi's [25] effective stress equation at full saturation and incompressible solids,

$$\boldsymbol{\sigma}' = \boldsymbol{\sigma} + p_{\mathrm{w}}\mathbf{1}\,. \tag{44}$$

Thus, equation (37) is a complete effective stress equation for partially saturated porous materials capable of reproducing other well-known forms of the effective stress equation under special conditions.

That $\boldsymbol{\sigma}'$ is a complete effective stress tensor may be seen from equation (36), which contains the term $\boldsymbol{\sigma}' : \boldsymbol{d}$ plus other terms that are not related to the deformation of the solid phase. If, on the other hand, we define the 'effective stress' as

$$\boldsymbol{\sigma}'' = \boldsymbol{\sigma} + \left[\psi^{\mathrm{w}}p_{\mathrm{w}} + (1 - \psi^{\mathrm{w}})p_{\mathrm{a}}\right]\mathbf{1}\,, \tag{45}$$

then we see that

$$\boldsymbol{\sigma}' : \boldsymbol{d} = \boldsymbol{\sigma}'' : \boldsymbol{d} - \frac{K}{K_{\mathrm{s}}}\overline{p}\mathbf{1} : \boldsymbol{d}\,. \tag{46}$$

Therefore, $\boldsymbol{\sigma}''$ cannot represent the work done in compressing the solid constituent itself. Finally, if we consider the familiar net stress tensor

$$\boldsymbol{\sigma}_{\mathrm{net}} = \boldsymbol{\sigma} + p_{\mathrm{a}}\mathbf{1}\,, \tag{47}$$

then we see that

$$\boldsymbol{\sigma}' : \boldsymbol{d} = \boldsymbol{\sigma}_{\mathrm{net}} : \boldsymbol{d} - \left(\psi^{\mathrm{w}}s + \frac{K}{K_{\mathrm{s}}}\overline{p}\right)\mathbf{1} : \boldsymbol{d}\,. \tag{48}$$

We see that $\boldsymbol{\sigma}_{\mathrm{net}}$ has many more terms in the energy equation that it cannot represent, including the energy produced by the suction stress s that also

depends on the rate of deformation of the solid matrix. On a related note, it is well known that the position of the critical state line for unsaturated soils generally varies with the suction stress when one uses the net stress in the constitutive description [20]. This is precisely due to the incomplete nature of the net stress as shown above, in that it cannot represent the energy produced by the suction stress in deforming the solid matrix.

4 Formulation of boundary-value problem

It is possible to formulate a complete boundary-value problem incorporating all of the elements presented in the previous section. However, we can simplify the formulation considerably by ignoring some terms that likely will not be relevant for the problem at hand. For example, for shallow, non-dynamic solid deformation we can set $p_a = 0$ (i.e., atmospheric). Furthermore, $B = 1.0$ (incompressible solid) and $K_w \to \infty$ (incompressible water constituent) are realistic assumptions for most geotechnical applications. We can also ignore the mass of air, so that balance of linear momentum in a given unsaturated porous domain $\mathcal{B}$ can be written simply as

$$\boldsymbol{\nabla} \cdot (\boldsymbol{\sigma}' - \psi^w p \mathbf{1}) + \rho \boldsymbol{g} = \mathbf{0}\,, \qquad \rho = \phi^s \rho_s + \phi^w \rho_w\,, \tag{49}$$

where $\boldsymbol{\sigma}'$ is the effective Cauchy stress tensor defined in (37), and $p \equiv p_w$ for brevity. Balance of water mass in the subsurface takes the form

$$(1 - \phi^s)\dot{\psi}^w + \psi^w \boldsymbol{\nabla} \cdot \boldsymbol{v} + \boldsymbol{\nabla} \cdot \boldsymbol{q} = 0\,, \tag{50}$$

where $\boldsymbol{q} = \phi^w \widetilde{\boldsymbol{v}}_w$ is the relative discharge velocity and the superimposed dot is the material time derivative following the solid motion.

To complete the presentation of the governing equations, we need to make some constitutive assumptions. First, we assume that the relative discharge velocity is governed by the generalized Darcy's law of the form

$$\boldsymbol{q} = k_{rw} \boldsymbol{K} \cdot \boldsymbol{\nabla} \left(\frac{p}{\rho_w g} + z \right)\,, \tag{51}$$

where $\boldsymbol{K}$ is the hydraulic conductivity of the porous medium at complete saturation, k_{rw} is the relative permeability that varies with degree of saturation ψ^w, g is the gravity acceleration constant, and z is the vertical coordinate. Furthermore, we assume two additional constitutive laws relating the Cauchy effective stress rate tensor $\dot{\boldsymbol{\sigma}}'$ with the strain rate tensor $\boldsymbol{\nabla}^s \boldsymbol{v}$ for the solid matrix, and the suction stress $s = -p$ with degree of saturation ψ^w. The latter constitutive law may be determined experimentally from the soil-water retention curve, which we express below using the van Genuchten equation [26] as

$$\psi^w(s) = \psi_1 + (\psi_2 - \psi_1)\left[1 + \left(\frac{s}{s_a}\right)^n\right]^{-m}\,. \tag{52}$$

The above equation contains four parameters: ψ_1 is the residual water saturation, ψ_2 is the maximum water saturation, s_a is a scaling pressure, and n and m are empirical constants defining the shape of the saturation curve. The constants n and m are not independent, but are rather related to one another as

$$m = \frac{n-1}{n} \,. \tag{53}$$

The water phase relative permeability is similarly defined as

$$k_{\mathrm{rw}}(\theta) = \theta^{1/2} \left[1 - \left(1 - \theta^{1/m} \right)^m \right]^2 , \qquad \theta = \frac{\psi^{\mathrm{w}} - \psi_1}{\psi_2 - \psi_1} \tag{54}$$

Finally, the material time derivative of degree of saturation can be expressed in terms of the material time derivative of suction as

$$\dot{\psi}^{\mathrm{w}} = \Psi \dot{s} = -\Psi \dot{p} \,, \qquad \Psi = \psi^{\mathrm{w}\prime}(s) \,. \tag{55}$$

Thus, we see that the governing equations (49) and (50) can be expressed in terms of two independent variables alone, namely, the solid velocity $\boldsymbol{v} \equiv \dot{\boldsymbol{u}}$ and pore water pressure p. The solution is fully coupled in the sense that the independent variables are determined simultaneously.

We complete the statement of the problem by specifying appropriate boundary and initial conditions. To this end, we assume that the total boundary $\partial\mathcal{B}$ of domain $\mathcal{B}$ can be decomposed as follows

$$\partial\mathcal{B} = \overline{\partial\mathcal{B}_{\boldsymbol{u}} \cup \partial\mathcal{B}_{\boldsymbol{t}}} = \overline{\partial\mathcal{B}_p \cup \partial\mathcal{B}_q} \,, \tag{56}$$

$$\varnothing = \partial\mathcal{B}_{\boldsymbol{u}} \cap \partial\mathcal{B}_{\boldsymbol{t}} = \partial\mathcal{B}_p \cap \partial\mathcal{B}_q \,, \tag{57}$$

where $\partial\mathcal{B}_{\boldsymbol{u}} = $ solid displacement boundary, $\partial\mathcal{B}_{\boldsymbol{t}}$ solid traction boundary, $\partial\mathcal{B}_p = $ fluid pressure boundary, $\partial\mathcal{B}_q = $ fluid flux boundary. The boundary conditions are then given as

$$\begin{aligned}
\boldsymbol{u} &= \overline{\boldsymbol{u}} & \text{on } \partial\mathcal{B}_{\boldsymbol{u}} \,, & \tag{58} \\
\boldsymbol{n} \cdot \boldsymbol{\sigma} &= \overline{\boldsymbol{t}} & \text{on } \partial\mathcal{B}_{\boldsymbol{t}} \,, & \tag{59} \\
p &= \overline{p} & \text{on } \partial\mathcal{B}_p \,, & \tag{60} \\
-\boldsymbol{n} \cdot \boldsymbol{q} &= \overline{q} & \text{on } \partial\mathcal{B}_q \,. & \tag{61}
\end{aligned}$$

The initial conditions are given as

$$\boldsymbol{u}(\boldsymbol{x}, t = 0) = \boldsymbol{u}_0 \,, \qquad p(\boldsymbol{x}, t = 0) = p_0 \,, \tag{62}$$

for all $\boldsymbol{x} \in \mathcal{B}$.

Following standard lines, we consider two spaces of trial functions defined as

$$\mathcal{U} = \{ \boldsymbol{u} : \mathcal{B} \to R^3 \,|\, u_i \in H^1, \boldsymbol{u} = \overline{\boldsymbol{u}} \text{ on } \partial\mathcal{B}_{\boldsymbol{u}} \} \,, \tag{63}$$

$$\mathcal{P} = \{ p : \mathcal{B} \to R^3 \,|\, p \in H^1, p = \overline{p} \text{ on } \partial\mathcal{B}_p \} \,, \tag{64}$$

where H^1 denotes a Sobolev space of degree one. We also define the corresponding spaces of variations,

$$\mathcal{U}^* = \{\boldsymbol{\eta} : \mathcal{B} \to R^3 \,|\, \eta_i \in H^1, \boldsymbol{\eta} = \boldsymbol{0} \text{ on } \partial\mathcal{B}_{\boldsymbol{u}}\} \,, \tag{65}$$

$$\mathcal{P}^* = \{\theta : \mathcal{B} \to R^3 \,|\, \pi \in H^1, \theta = 0 \text{ on } \partial\mathcal{B}_p\} \,. \tag{66}$$

The weak form of the problem is then to find $\{\boldsymbol{u}, p\} \in \mathcal{U} \times \mathcal{P}$ such that for all $\{\boldsymbol{\eta}, \theta\} \in \mathcal{U}^* \times \mathcal{P}^*$, balance of momentum,

$$\int_{\mathcal{B}} \boldsymbol{\nabla}^{\mathrm{s}} : \boldsymbol{\sigma}' \, \mathrm{d}V - \int_{\mathcal{B}} \boldsymbol{\nabla} \cdot \boldsymbol{\eta} \psi^{\mathrm{w}} p \, \mathrm{d}V - \int_{\mathcal{B}} \boldsymbol{\eta} \cdot \rho\boldsymbol{g} \, \mathrm{d}V - \int_{\partial\mathcal{B}_{\boldsymbol{t}}} \boldsymbol{\eta} \cdot \bar{\boldsymbol{t}} \, \mathrm{d}A = 0 \tag{67}$$

and balance of mass

$$-\int_{\mathcal{B}} \theta\psi^{\mathrm{w}} \boldsymbol{\nabla} \cdot \dot{\boldsymbol{u}} \, \mathrm{d}V - \int_{\mathcal{B}} \theta(1 - \phi^{\mathrm{s}})\dot{\psi}^{\mathrm{w}} \, \mathrm{d}V + \int_{\mathcal{B}} \boldsymbol{\nabla}\theta \cdot \boldsymbol{q} \, \mathrm{d}V + \int_{\partial\mathcal{B}_q} \theta\bar{q} \, \mathrm{d}A = 0 \tag{68}$$

hold. Note in the above variational equation that we have left the term $\dot{\psi}^{\mathrm{w}}$ as is, instead of replacing it with $-\Psi\dot{p}$ as was done in (55). In general, the saturation-suction relation is highly nonlinear, and using the tangent $\Psi = \psi^{\mathrm{w}\prime}(s)$ can lead to large mass balance errors in the time-discrete setting as pointed out in [11]. Instead of using the tangent Ψ, we have thus used a direct backward implicit time-integration on the saturation in the form $\dot{\psi}^{\mathrm{w}}_{n+1} \approx (\psi^{\mathrm{w}}_{n+1} - \psi^{\mathrm{w}}_n)/\Delta t$, which leads to more desirable stability properties [28].

The above equations show the tight coupling that exists between the two degrees of freedom $\boldsymbol{u}$ and p. In the fully saturated range, this tight coupling is somewhat alleviated by noting that the variational equation for the balance of mass simplifies to [2]

$$-\int_{\mathcal{B}} \theta\boldsymbol{\nabla} \cdot \dot{\boldsymbol{u}} \, \mathrm{d}V + \int_{\mathcal{B}} \boldsymbol{\nabla}\theta \cdot \boldsymbol{q} \, \mathrm{d}V + \int_{\partial\mathcal{B}_q} \theta\bar{q} \, \mathrm{d}A = 0 \,. \tag{69}$$

However, the two primary variables, $\boldsymbol{u}$ and p, are still linked together and must be determined simultaneously.

Mixed finite element (FE) equations may be readily developed from the above variational equations. The independent variables are the nodal displacement vector $\boldsymbol{d}$ and nodal pore water pressure vector $\boldsymbol{p}$. The coupled FE equations take the form

$$\boldsymbol{F}_{INT}(\boldsymbol{d}) + \boldsymbol{G}\boldsymbol{p} \;\;=\;\; \boldsymbol{F}_{EXT} \,, \tag{70}$$

$$\boldsymbol{G}^{\mathsf{T}}\dot{\boldsymbol{d}} + \boldsymbol{\Psi}(\boldsymbol{p}) + \boldsymbol{\Phi}\boldsymbol{p} \;\;=\;\; \boldsymbol{G}_{EXT} \,, \tag{71}$$

where $\boldsymbol{F}_{INT}(\boldsymbol{d})$ is the internal nodal force vector arising from the effective stress $\boldsymbol{\sigma}'$, $\boldsymbol{G}$ and $\boldsymbol{G}^{\mathsf{T}}$ are the discrete gradient and discrete divergence operators, respectively, which depend on $\boldsymbol{p}$ through the degree of saturation ψ^{w} in the unsaturated regime, $\boldsymbol{\Psi}(\boldsymbol{p})$ is a nonlinear vector function of the pressure resulting from direct time-integration of the rate of saturation (which
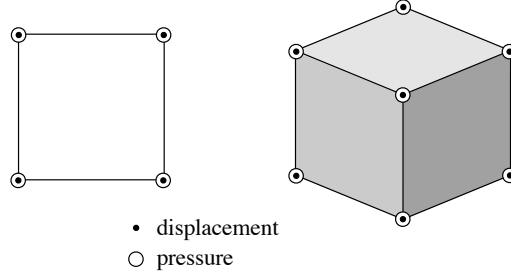
- • displacement
- ○ pressure

Fig. 1. Stabilized low-order mixed finite elements for coupled solid-deformation/fluid-diffusion: four-node quadrilateral for 2D (left), and eight-node hexahedral for 3D (right). After References [9, 27].

vanishes at full saturation), $\boldsymbol{\Phi}$ is an effective conductivity matrix that also depends on the degree of saturation, and $\boldsymbol{F}_{EXT}$ and $\boldsymbol{G}_{EXT}$ are prescribed vectors of momentum and fluid supplies. The degree of coupling implied by the above equations is more intricate than in the fully saturated case because of the presence of ψ^{w} in many places, which produces additional terms in the derivatives relevant for Newton iteration.

As noted in the Introduction, we shall focus specifically on low-order mixed finite elements, such as the 2D quadrilateral and 3D hexahedral elements shown in Fig. 1. Higher-order elements could be prohibitively expensive and may not be so useful for problems dominated by spatially varying material properties and irregular geometric conditions [13]. The mixed finite elements shown in Fig. 1 employ equal-order interpolation for displacement and pressure fields (bilinear for 2D and trilinear for 3D), which work well under normal drainage loading conditions, but they could produce problematic pressure oscillations in the limit of full saturation and undrained loading. This numerical instability is well known and can be attributed to the failure of the equal-order pair to satisfy the discrete LBB condition [10]. A technique based on polynomial pressure projection has been shown to work for Stokes and Darcy equations [4, 5, 12], as well as for coupled solid deformation-fluid diffusion problems involving full and partial saturation [9, 27]. The stabilized hexahedral mixed element shown in Fig. 1 is used in the 3D simulations described in the next section.

5 Numerical example

We consider an earthen embankment loaded by an upstream reservoir (Figs. 2 and 3). The embankment has a somewhat complicated three-dimensional structure due to its siting in a shallow valley. Parallel to the y-axis, the embankment spans the valley with a 1:4 slope. Parallel to the x-axis, the
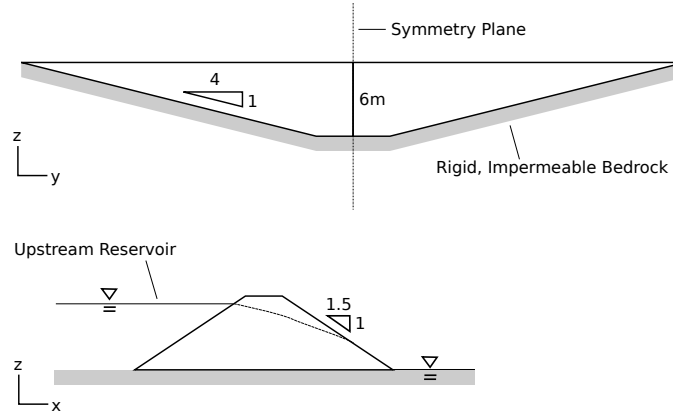
Fig. 2. Geometry and boundary conditions for a 3D embankment analysis.

upstream and downstream faces of the embankment have a 1:2 slope. At its deepest point, the embankment is 6 m tall. We remark that in this case it would likely be insufficient to model just a 2D slice through the centerline of the structure. The geometry implies that both the fluid flow and deformation may deviate significantly from any sort of plane-flow, plane-strain assumptions.

The structure is founded on rigid, impermeable bedrock and therefore no-slip, no-flux boundary conditions are assigned at these faces. From the inherent symmetry in the problem, it is only necessary to model half of the domain. On the symmetry plane, we assign no-normal-displacement and no-flux boundary conditions. A convenient consequence of modeling only half the domain is that we can immediately view a cross-section of the solution through the centerline of the embankment. For the mesh, we use low-order Lagrangian hexahedra. Note that for clarity Fig. 3 only presents a coarse version of the gridding, while the actual computations were run on a more refined mesh. The actual mesh has 54,000 elements and 234,484 total degrees of freedom (175,863 displacement degrees and 58,621 pressure degrees). The mesh has a structured topology, though of course more general unstructured meshes could also be considered.

The soil in the embankment is modeled using a non-associative Drucker-Prager elastoplasticity model. The Drucker-Prager model uses a two-invariant, pressure-dependent yield surface that can be thought of as a smoothed version of the classic Mohr-Coulomb model. To calibrate the yield surface and plastic potential, three-parameters are required: the soil cohesion, friction angle, and dilatancy angle. All three may be determined from standard laboratory tests. For simplicity we ignore any hardening or softening behavior in the cohesive or frictional behavior. Inside the yield surface, linear elastic behavior is defined using a bulk modulus and Poisson's ratio for the soil. We remark that while the Drucker-Prager model is simple to calibrate and is sufficient for our purposes
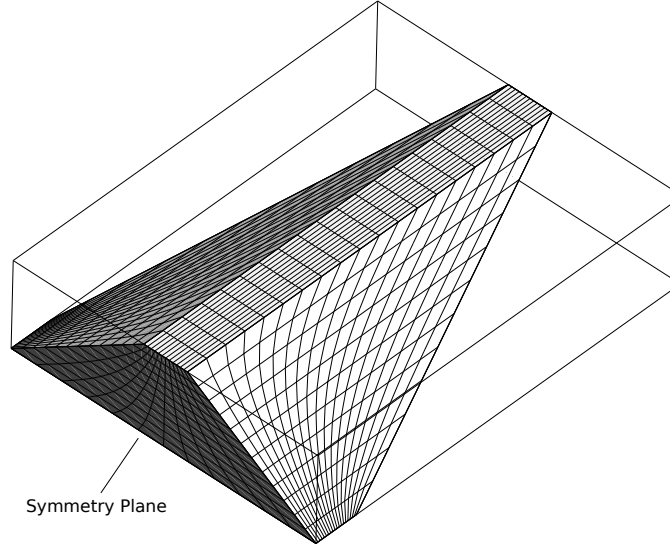
Symmetry Plane

Fig. 3. Mesh used for the embankment analysis. From symmetry, only half the domain is discretized. For clarity, only a coarse version of the mesh is shown.

here, it ignores many features of typical soil behavior that can be captured by more sophisticated models. For example, a cap model limiting the elastic region on the compression side could lead to a yield stress that depends on the suction stress [1, 14, 16, 20]. Drucker-Prager plasticity, however, is appropriate for yielding on the dilative side where the influence of suction on the yield stress may not be as apparent. Still, even though the yield stress for such material does not depend directly on suction, the constitutive model itself is expressed in terms of the proposed effective stress that depends on the capillary pressure.

We refer the interested reader to the extensive literature on soil constitutive modeling, including several valuable contributions on unsaturated soils in this book. For the flow response, the model requires relative-permeability and saturation relationships, for which we use a van Genuchten [1980] model. These relationships are plotted in Fig. 4. For ease of reference, all of the model parameters are collected in Table 1.

We now consider the water table behavior on either side of the embankment. On the downstream side, the water table is fixed at $z = 0$ m, while on the upstream side the reservoir level $h(t)$ is allowed to vary with time. In particular, we assume the following variation of water elevation on the upstream side of the embankment:
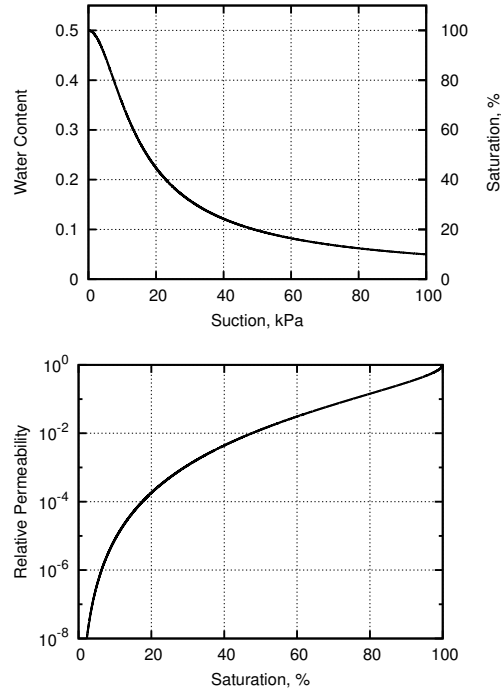
Fig. 4. Suction/saturation and saturation/relative permeability relationships for the embankment soil.

$$
h(t) = \begin{cases}
0 & t \leq 0 \\
0.1t & 0 < t \leq 50 \\
5.0 & 50 < t \leq 100 \\
5.0 - 0.1t & 100 < t \leq 150 \\
0 & t > 150,
\end{cases}
\tag{72}
$$

where h is in meters and t is in hours. That is, the reservoir is initially empty, but is slowly raised to 5 m over 50 hrs, after which it is held constant for another 50 hrs before being drained again. The changing reservoir conditions will lead to complicated infiltration and exfiltration conditions on both upstream and downstream faces of the structure, as well as changing traction conditions on the upstream face.

At the beginning of the simulation, the embankment is assigned a hydrostatic pressure profile, consistent with water table level on either side. The entire embankment is therefore unsaturated, with a capillary fringe determined by the suction/saturation model. To determine the initial geostatic stress state, the soil is first allowed to consolidate under its own self-weight during a gravity-loading phase. With the initial stress state computed, the

Table 1. Model parameters used for the embankment example.

Porosity	$1 - \phi^{\mathrm{s}}$	0.5	—
Solid Density	ρ_{s}	2.0	$\mathrm{Mg/m^3}$
Fluid Density	ρ_{w}	1.0	$\mathrm{Mg/m^3}$
Bulk Modulus	K	10.0	MPa
Poisson Ratio	ν	0.2	—
Cohesion	c	2.0	kPa
Friction Angle	ϕ	28.0	deg.
Dilatancy Angle	ψ	10.0	deg.
Intrinsic Permeability	k	10^{-12}	$\mathrm{m^2}$
Dynamic Viscosity	μ	10^{-6}	kPa·s
Residual Saturation	ψ_1	0	—
Maximum Saturation	ψ_2	1.0	—
Scaling Suction	s_a	10.0	kPa
vG Parameter	n	2.0	—
vG Parameter	m	0.5	—

displacements are then reset to zero and the coupled hydromechanical portion of the simulation begins. All time-integration calculations were carried out using the backward implicit scheme.

First, we examine the hydrologic response. Figure 5 shows snapshots of the saturation profile within the embankment at several timesteps. As the water level in the reservoir rises over the first 50 hrs, the upstream face of the embankment saturates, and a wetting front gradually moves towards the downstream toe. Because the water table on the downstream side is held fixed, a seepage face eventually forms in order to accommodate the flux through the dam. The time-scale of loading is too short, however, for a steady-state profile to develop. At 100 hrs, the reservoir is drawn down and we observe a lowering of the phreatic surface. The drawdown is too rapid, however, for the phreatic surface to remain in equilibrium with the upstream reservoir level, and we observe the formation of a second seepage face on the upstream side of the dam. Over the course of the drawdown, the height of the downstream seepage face also continues to grow. This simulation illustrates the complicated boundary conditions that may be encountered in a typical application, with exterior faces switching back and forth between fixed pressure and fixed flux depending on the external loading and internal pressure state. Also note that the saturation contours are fully three-dimensional, due to interaction with the sloping valley floor. Indeed, there is significant flow convergence due to this geometry.

We now consider the solid response. Note that the upstream reservoir has a variety of effects on the soil in the embankment. As just noted, the
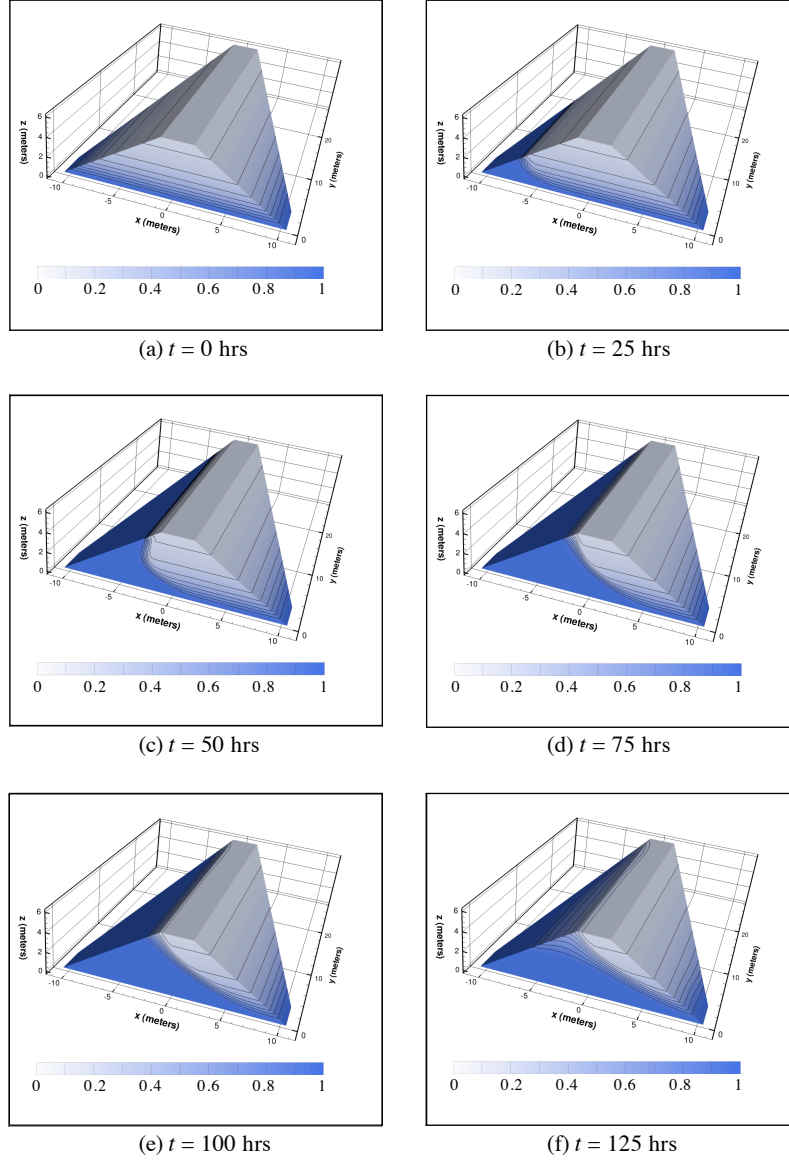
(a) $t = 0$ hrs

(b) $t = 25$ hrs

(c) $t = 50$ hrs

(d) $t = 75$ hrs

(e) $t = 100$ hrs

(f) $t = 125$ hrs

Fig. 5. Snapshots of saturation contours in the embankment over the course of the simulation. Color bar is degree of saturation in decimals.

hydrostatic pressure of the reservoir determines the fluid pressure condition at the upstream interface. This leads to increasing positive pressures in the embankment, which in turn reduce the effective stress in the soil skeleton.
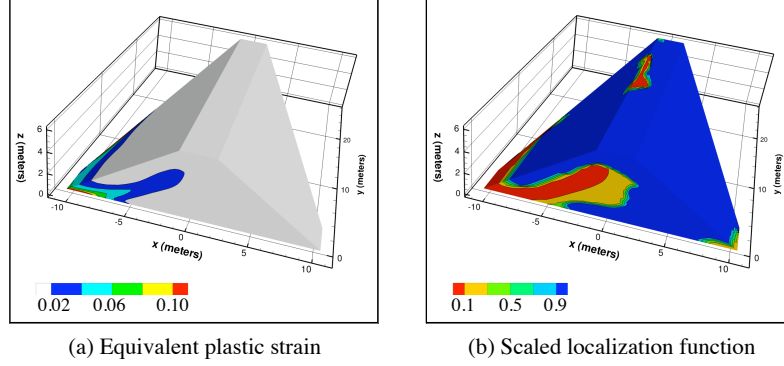
(a) Equivalent plastic strain   (b) Scaled localization function

Fig. 6. Contours of: (a) equivalent plastic strain in percent, and (b) scaled localization function at $t = 133$ hrs, showing the formation of an incipient failure surface on the upstream face due to the reservoir drawdown.

Also, recall that the effective density of the soil changes with saturation, as the skeleton begins to experience buoyant forces. These effects combine to lower the shear resistance of the soil. On the other hand, the weight of the reservoir exerts a normal (total) traction on the upstream face, which ensures that the soil remains stable. The importance of this normal traction is seen as soon as the reservoir is drawn down. When the reservoir level drops, the weakened soil in the dam is no longer properly confined and we observe the initiation of a slope failure. Figure 6a illustrates contours of equivalent plastic strain at 133 hrs, in which we see the beginning of shear localization at the base, which gradually grows upward. The potential for shear localization is also seen when plotting the scaled localization function [22] (Figure 6b). In the vicinity of the shear band the localization function approaches the zero-threshold value for bifurcation and loss of stability. The use of the localization function is also interesting because it reveals other zones of weakness that are not immediately apparent from the plastic strain contours. Indeed, we observe the potential for shear localization at the downstream toe and near the far edge of the valley. Immediately after the 133 hr mark, a complete slip surface formed and a global collapse occurred. Note that the soil at the shallower edges of the valley is not subject to the same level of forcing as the deeper central portion, and remains stable. As a result, the failure surface has a complicated three-dimensional structure.

Although we have not considered this case here, it is also important to consider what might happen if the reservoir was kept at full height and the growth of the seepage face at the toe was allowed to continue. The downstream face is always unconfined and we might eventually observe a slope failure on

this face instead. The current embankment design does not contain any toe drains or a central core that might mitigate this effect.

It is interesting to compare the current analysis with more traditional slope stability methods. Perhaps the most obvious advantage is that it is fully three-dimensional, while many simplified approaches require examining a representative 2D slice. Second, it rigorously accounts for unsaturated flow and effective stress behavior. The scaling of the suction/saturation relationship used in this example is such that the embankment possesses a relatively large capillary fringe above the zero-pressure contour, and this vadose zone plays an important role in mechanics of the problem. Third, the simulation accounts for a tight-coupling between solid and fluid response. In principle, however, we could adopt an uncoupled analysis approach—first using a seepage simulation to predict a phreatic contour, and then a stress-deformation or method-of-slices analysis to examine the slope stability subject to the (now-fixed) pressure field. While we might be able to obtain a conservative estimate of the slope stability using this approach, it would ignore much of the time-dependent nature of the problem and any feedback effect of the solid deformation on the fluid flow. By necessity, such an uncoupled analysis must also make a variety of simplifying assumptions about the effective stress response, whereas the coupled model can accomodate much more sophisticated constitutive assumptions about the unsaturated soil behavior. Of course, there are disadvantages to the fully-coupled approach. The simulations are computationally more expensive, though growing computer power and intelligent solver design can mitigate much of this concern. Also, a more sophisticated model generally requires more material parameters that must be calibrated from experiments. Finally, it is difficult to assign a single metric of performance like factor-of-safety to such an analysis, which is an appealing concept from a design and practice point of view. Nevertheless, none of these disadvantages is severe, and they are perhaps the price of a more meaningful representation of the underlying physics.

6 Closure

We have presented conservation laws governing the hydro-mechanical processes in unsaturated porous media using continuum mixture theory. From the first law of thermodynamics, we have identified a complete effective stress measure appropriate for constitutive modeling of the solid matrix. We have used this effective stress measure for stating the initial boundary-value problem for coupled solid deformation-fluid diffusion in unsaturated porous media, and for numerical implementation of the conservation laws based on mixed finite element formulation. We have investigated the low-order quadrilateral elements in 2D and hexahedral elements in 3D employing equal order interpolation of displacement and pore pressure fields, identified their stability (or lack of it) properties in the regime of full saturation and undrained loading,

and introduced stabilization schemes so that these elements may be used effectively for the simulation of boundary-value problems for the entire range of drainage and saturation conditions. The 3D numerical example presented in this paper well illustrates the advances in large-scale simulation of coupled solid deformation-fluid diffusion analysis employing the proposed mixed finite element technique, as well as illustrates the potential challenges for accommodating more complex conditions including large deformation and more elaborate constitutive models for application to unsaturated porous media problems.

Acknowledgements

References

[1] Alonso EE, Gens A, Josa A (1990) A constitutive model for partially saturated soils. Géotechnique 40:405–430
[2] Andrade JE, Borja RI (2007) Modeling deformation banding in dense and loose fluid-saturated sands. Finite Elements in Analysis and Design 43:361–383
[3] Bishop AW (1959) The principle of effective stress. Teknisk Ukeblad 39:859–863
[4] Bochev PB, Dohrmann CR, Gunzburger MD (2006) Stabilization of low-order mixed finite elements for the Stokes equations. SIAM Journal for Numerical Analysis 44:82–101
[5] Bochev PB, Dohrmann CR (2006) A computational study of stabilized, low-order C^0 finite element approximations of Darcy equations. Computational Mechanics 38:323–333
[6] Borja RI (2004) Cam-Clay plasticity, Part V: A mathematical framework for three-phase deformation and strain localization analyses of partially saturated porous media. Computer Methods in Applied Mechanics and Engineering 193:5301–5338
[7] Borja RI (2006) On the mechanical energy and effective stress in saturated and unsaturated porous continua. International Journal of Solids and Structures 43:1764–1786

[8] Borja RI, Koliji A (2009) On the effective stress in unsaturated porous continua with double porosity, Journal of the Mechanics and Physics of Solids 57:1182–1193

[9] Borja RI, White JA (2010) Continuum deformation and stability analyses of a steep hillside slope under rainfall infiltration, Acta Geotechnica, doi: 10.1007/s11440-009-0108-1

[10] Brezzi F (1990) A discourse on the stability conditions for mixed finite element formulations, Computer Methods in Applied Mechanics and Engineering 82:27–57.

[11] Celia M, Bouloutas E, Zarba R (1990) A general mass-conservative numerical solution for the unsaturated flow equation, Water Resources Research 26:1483–1496

[12] Dohrmann CR, Bochev PB (2004) A stabilized finite element method for the Stokes problem based on polynomial pressure projections. International Journal for Numerical Methods in Fluids 46:183–201

[13] Ehlers W, Ammann M, Diebels S (2002) h-Adaptive FE methods applied to single-and multiphase problems. Int. J. Numer. Meth. Eng., 54:219–239

[14] Gallipoli G, Gens A, Sharma R, Vaunat J (2003) An elasto-plastic model for unsaturated soil incorporating the effects of suction and degree of saturation on mechanical behavior, Géotechnique 53:123–135

[15] Houlsby GT (1997) The work input to an unsaturated granular material. Géotechnique 47:193–196

[16] Khalili N, Geiser F, Blight GE (2004) Effective stress in unsaturated soils: review with new evidence. International Journal of Geomechanics 4:115–126

[17] Lambe TW, Whitman RV (1969) Soil Mechanics. John Wiley % Sons, New York

[18] Lu N, Likos WJ (2004) Unsaturated Soil Mechanics, John Wiley & Sons, Inc., Hoboken, New Jersey

[19] Nur A, Byerlee JD (1971) An exact effective stress law for elastic deformation of rock with fluids. Journal of Geophysical research 76:6414–6419

[20] Nuth M, Laloui L (2008) Effective stress concept in unsaturated soils: Clarification and validation of a unified framework. International Journal for Numerical and Analytical Methods in Geomechanics 32:771–801

[21] Richards LA (1931) Capillary conduction of liquids in porous mediums. Physics 1:318–333

[22] Rudnicki JW, Rice JR (1975) Conditions for the localization of deformation in pressure-sensitive dilatant materials. Journal of the Mechanics and Physics of Solids 23:371–394

[23] Schrefler BA (1984) The finite element method in soil consolidation (with applications to surface subsidence), Ph.D. Thesis, University College of Swansea, C/Ph/76/84

[24] Skempton AW (1961) Effective stress in soils, concrete and rocks. In: Pore Pressure and Suction in Soils, Butterworths, London, pp. 4–16

[25] Terzaghi K (1943) Theoretical Soil Mechanics. John Wiley and Sons, New York, NY

[26] Van Genuchten MT (1980) A closed-form equation for predicting the hydraulic conductivity of unsaturated soils. Soil Science Society of America Journal 44:892–898

[27] White JA, Borja (2008) Stabilized low-order finite elements for coupled solid-deformation/fluid-diffusion and their application to fault zone transients. Computer Methods in Applied Mechanics and Engineering 197:4353–4366

[28] White JA (2009) Stabilized Finite Element Methods for Coupled Flow and Geomechanics, Ph.D. Thesis, Stanford University, Stanford, California, USA.